International Journal of Heat and Mass Transfer 52 (2009) 3128–3136

Contents lists available at ScienceDirect

International Journal of Heat and Mass Transfer

journal homepage: www.elsevier.com/locate/ijhmt

Numerical study of forced turbulent heat convection in a straight square duct

Hongxing Yang *, Tingyao Chen, Zuojin Zhu[1]

Department of Building Services Engineering, The Hong Kong Polytechnic University, Kowloon, Hung Hom, Hong Kong, PR China

ARTICLE INFO

Article history:
Received 2 October 2008
Received in revised form 10 January 2009
Accepted 10 January 2009
Available online 26 March 2009

Keywords:
Forced turbulent heat convection
Straight square duct
Nonstandard analysis of turbulence
Passive scalar

ABSTRACT

This paper presents the coarse-grid direct numerical simulation (c-DNS) of forced turbulent heat convection in a straight square duct (SSD) at a bulk Reynolds number of 10^4. The temperature was considered as a passive scalar due to the neglect of the buoyancy effect. This c-DNS based on the recent nonstandard analysis of turbulence was carried out in a staggered grid system with a projection method on the basis of finite difference. To reduce numerical errors due to the staggered grid arrangement and enhance the finite difference accuracy, the grid-dependent interpolation remainders were derived in the calculation of cross-convection velocities by using Taylor expansion. These remainders were used to design an improved fourth-order upwind scheme for the finite difference of convection terms. The c-DNS results show that the novel numerical scheme can give satisfactory solutions of the turbulent SSD flow with passive scalar transport under an isoflux condition. The predicted mean Nusselt number is excellently consistent with the value based on the published correlations. The effect of the mean secondary flow can significantly increase the ratio between the temperature and velocity dissipation time scales in the corner region between the mean secondary counter-rotating vortices.

1. Introduction

The forced turbulent heat convection in a straight square duct (SSD) is one of the fundamental problems in thermal science and fluid mechanics. This forced heat convection is dominated by the turbulent flow in the SSD, which has a remarkable change in flow structure due to the existence of the so-called Prandtl's second kind secondary flows [1]. Such Prandtl's second kind secondary flow has a significant effect on the transport of heat and momentum as revealed by the recent large eddy simulation (LES) [2].

As revealed by early measurements [3], the independent secondary flow circulation zones are separated by the corner bisectors, but the flow pattern is not so complex as inferred from the distortion of the longitudinal flow. The secondary-flow velocities decrease with Reynolds number when they are normalized by either the bulk mean velocity or the axial mean-flow velocity at the channel centreline. Further work [4] has shown that in the planes normal to the axial flow direction, traces of Reynolds stress on principal planes are not tangent and normal to lines of constant axial mean-flow velocity. The secondary flow is the result of small differences in magnitude of opposing forces exerted by the Reynolds stresses and static pressure gradients on planes normal to the axial flow direction. Other experimental results for the SSD flow can be found in Refs. [5,6].

Among the flow simulations, to calculate the fully developed turbulent flows in square, rectangular and trapezoidal ducts, an algebraic stress model for the secondary flow of the second kind with the $k-\epsilon$ model was used by Nakayama et al. [7], emphasizing the local structures of turbulence to reveal full features of the turbulence model. The turbulent convective heat transfer in a SSD has been a hot topic in the numerical studies, some examples can be found in the work based on the algebraic stress model of turbulence [8], in those focusing on the effect of rib roughened wall [9–11], and on the effect of a square bar detached from the wall [12].

The recent contributions to computational fluid dynamics were those using large eddy simulation(LES) [13–19] and direct numerical simulation (DNS) [20–23]. In particular, Vázquez and Métais [15] predicted the asymmetrical wall heating and the fluid compressibility effects. For the case of strongest heating, near the heated wall, a saturation of the spanwise wavelength of the streaky system could be observed. Studies on turbulent channel flows by computations [24–30], and by experiments [31–34] have been carried out, since the earlier DNS [20] indicated that turbulent statistics along the wall bisectors agrees well with plane channel data despite the influence of the sidewalls in the former flow.

As reported in our previous work [35,36], the traditional means of DNS should use a very fine grid system causing the computational demands exceed the capability of a personal computer, we

* Corresponding author.
E-mail addresses: behxyang@polyu.edu.hk (H. Yang), betychen@polyu.edu.hk (T. Chen).
URL: http://staff.ustc.edu.cn/~zuojin (Z. Zhu).
[1] Multiphase Reactive Flow Division, Department of Thermal Science and Energy Engineering, USTC, Hefei 230026, PR China.

0017-9310/$ - see front matter © 2009 Elsevier Ltd. All rights reserved.
doi:10.1016/j.ijheatmasstransfer.2009.01.029

Nomenclature

A, B, C, D	coefficients of finite difference
C_D	coefficient in turbulence model
c_p	specific heat at constant pressure (J/kg K)
f	mean friction factor
H	duct section side length
I	linear interpolation operator
k_u	turbulence kinetic energy
k_θ	temperature variance
$\overline{Nu}_{av}$	mean Nusselt number in Eq. (9)
p	normalized pressure
Pr	Prandtl number
Q_w	heat transfer rate per unit area (W/m^2)
$\mathbf{u}$	normalized velocity vector
R	time ratio in Eq. (17)
Re	balk mean Reynolds number
Re_τ	friction Reynolds number
T	temperature
T_τ	mean friction temperature (K)
u, v, w	normalized velocity components
U_m	balk mean velocity (m/s)
u_τ	mean friction velocity (m/s)
x, y, z	Cartesian coordinates
y^+	$= (y + 0.5)u_\tau/\nu$, wall coordinate
Θ^+	$\equiv \theta^+/13$, normalized temperature
ν	kinematic viscosity of fluid (m^2/s)
ϵ_u	dissipation rate of k_u
ϵ_θ	dissipation rate of k_θ
τ_u	velocity dissipation time scale
τ_θ	temperature dissipation time scale

incline to believe that the nonstandard analysis of turbulence presented by Wu [37–39] is more computationally efficient. This nonstandard analysis allows the use of c-DNS to obtain relatively accurate results. This suggests that the c-DNS is a promising technique in computational fluid dynamics(CFD) as proved by the recent work [40].

This paper presents the c-DNS results of the forced turbulent heat convection in SSD at $\mathrm{Re} = 10^4$ in which the temperature was taken as a passive scalar and the buoyancy effect was completely ignored. The governing equations were solved numerically by a projection method based on a finite difference scheme [41], which was improved by increasing the accuracy in the calculation of cross-convection velocities. For the sake of convenience, it is assumed that the flow Mach number is lower so that the air flow can be taken as incompressible; the temperature dependence of the air thermal–physical properties can be ignored. Since heating was in a constant heat flux (isoflux) mode, there should be an additional term for streamwise-velocity-dependent source in the energy equation to reflect the isoflux heating effect, as done in the previous work [28]. In addition to the improvement of the upwind finite difference scheme, we also consider calculating the mean Nusselt number, and revealing of the statistical characteristics of turbulent flow in the c-DNS work.

2. Governing equations

We assume that the origin of the cartesian coordinate system is located at the central point of the computational domain, and $x(x_1)$, $y(x_2)$ and $z(x_3)$ represent the coordinates in the streamwise, transverse and spanwise directions. We further assume that the air flow in the SSD is heated under an isoflux condition, implying that the time-averaged wall heat flux does not change in the x-direction. This heating mode is equivalent to an assumption that the time-averaged wall temperature $\langle T_w \rangle$, should increase linearly in x-direction, due to the global heat balance for a fully developed thermal field. Therefore, the bulk mean temperature $\langle T_m \rangle$ should also increase linearly in the x-direction, i.e. $\partial\langle T_m\rangle/\partial x = \partial\langle T_w\rangle/\partial x = \text{const}$.

Let $13T_\tau$ denote the temperature scale, the dimensionless temperature is defined as:

$$\Theta^+ = (\langle T_w \rangle - T)/(13T_\tau) \equiv \theta^+/13 \tag{1}$$

where T_τ is the friction temperature defined by $Q_w/(\rho c_p u_\tau)$. The factor 13 is used for the convenience of synchronizing the computation, i.e. it allows the solution of temperature with the same time step used in the velocity calculation. Further choose the bulk mean velocity U_m and the side length H as the velocity and the length scales, let ρ denote the air density, the time and pressure scales should be H/U_m and ρU_m^2. The energy conservation shows that the dimensionless temperature Θ^+ satisfies

$$\Theta_t^+ + \mathbf{u}\cdot\nabla\Theta^+ - \frac{4u_\tau}{13U_m\int_A u dA}u = \frac{1}{\mathrm{RePr}}\nabla^2\Theta^+ \tag{2}$$

Here $dA = dydz$, is the element of cross-sectional area, u is the normalized streamwise velocity component, and u_τ is the mean friction velocity. The Reynolds number is based on U_m, H, and air kinematic viscosity ν, the air Prandtl number Pr is 0.71. The last term on the left-hand side of Eq. (2) corresponds to $-u\{\partial\langle T_w\rangle^+/\partial x\}/13$, as stated by Kasagi et al. [28] in case of turbulent channel flow.

On the other hand, according to the concepts of nonstandard analysis of turbulence [37–39], the governing equations of the monad mean velocities can be written as

$$\nabla\cdot\mathbf{u} = 0 \tag{3}$$

$$\mathbf{u}_t + \mathbf{u}\cdot\nabla\mathbf{u} = -\nabla p + \nabla^2\mathbf{u}/\mathrm{Re} + \Pi\delta_{i1} \tag{4}$$

where δ_{ij} is the Kronecker delta tensor, Π represents the mean pressure gradient in the x-direction, which can be adjusted dynamically to maintain the constant mass flux in the SSD flow [42]. The initial flow field is assumed to be laminar, and perturbed by an approach incorporating the initial acceleration effect. The streamwise periodic condition is used with the non-slip conditions on the duct walls. The normalized temperature Θ^+ is zero on the SSD walls, and should be identical to $[\mathrm{Pr}\cdot u/(13u_\tau/U_m)]$ as the initial condition of the temperature field.

3. Numerical method

The temperature and velocity governing equations (2)–(4) have the same form of the Navier–Stokes type equations. Hence, the existing numerical methods are still available, such as the Chebyshev polynomial algorithm [43], the finite-difference method in arbitrary curvilinear orthogonal coordinates [44], the commonly appreciated finite volume method as described by Patankar [45], and Papanicolaou and Jaluria [46], and the finite element method as those appreciated by Khanafer et al. [47]. However, because the generic characteristics of turbulence shows that the turbulent temperature and velocity fields must occur in the form of plateaux separated by sharp cliffs as observed in scalar turbulence [48], in turbulence prediction, it is therefore necessary to reduce the artificial error from discretization and computation. Otherwise, the arti-

ficial viscous effect will present a spurious diffusion to decrease the variable fluctuations. Therefore, in this numerical study of forced heat convection in turbulent regime, we recruit some grid-dependent terms to erase the artificial error in discretization, and increase the accuracy of the pressure potential calculation by dropping the iteration criterion to a level of about 10^{-8}.

The numerical solutions of the turbulent SSD flow with heat transfer were found with the accurate projection algorithm PmIII [49] in a non-uniform staggered grid system. The procedure of the numerical method has been briefly described elsewhere [50]. Here we further detail the approach of the term recruiting. In the previous simulation of flow around two identical square cylinders, a higher-order upwind scheme was described in a staggered grid system [41]. This scheme has been found to be available in the study of transitional wake flow at a Reynolds number of 250. It has however implicitly introduced some artificial diffusion and dispersion terms in the finite difference of the non-linear cross-convection terms, such as vu_y, and wu_z in the momentum equation for the velocity in the streamwise direction. These terms are grid dependent, and can be found by Taylor expansion. It is required to remove the effect from these grid-dependent terms so that the previously proposed higher-order upwind scheme can be more suitable for turbulence exploration.

We make an example of seeking them in the finite difference of the term vu_y. In the staggered grid system, since the velocity components $[u_{ijk}, v_{ijk}]$ are, respectively, located at grid points $(x_{i-1/2}, y_j, z_k)$, and $(x_i, y_{j-1/2}, z_k)$, in the case of $\hat{v}_{ijk}(x_{i-1/2}, y_j, z_k) \geqslant 0$, the improved higher-order upwind scheme can be written in the following form

$$(vu_y)_{ijk} = \hat{v}_{ijk}\left[-(A+B+C)u_{ijk} + Au_{i,j-1,k} + Bu_{i,j-2,k} + Cu_{i,j+1,k} - D(u_y^{(4)})_{ijk}\right] \tag{5}$$

when $\delta y_j = y_j - y_{j-1}$, $s_2 = (\delta y_{j-1} + \delta y_j)/\delta y_j$, and $s_3 = \delta y_{j+1}/\delta y_j$, the coefficients of the finite difference can be expressed as

$$B = \frac{s_3^3 + s_3^2}{\delta y_j \cdot \Delta}, \quad C = -\frac{s_2^2 - s_2^3}{\delta y_j \cdot \Delta}, \quad A = -Bs_2^2 - Cs_3^2 \tag{6}$$

and

$$D = [A(\delta y_j)^4 + B(\delta y_j + \delta y_{j-1})^4 + C(\delta y_{j+1})^4]/24 \tag{7}$$

where $\Delta = s_2 s_3 (s_2 - 1)(s_3 + 1)(s_2 + s_3)$. Using the Taylor expansion, it is easy to express the cross-convection velocity by an interpolation with operator I^{β}_{ijk} and a corresponding grid-dependent remainder, that means

$$\begin{aligned} \hat{v}_{ijk} &= I^{\beta}_{ijk}(v) - R_{ijk} + o(\epsilon^4) \\ R_{ijk} &= \left\{(\delta x_i)^2 I^{\beta}_{ijk}(v_{xx}) + (\delta y_j \delta y_{j+1}) I^{\beta}_{ijk}[v_{yy} + (\delta y_{j+1} - \delta y_j) v_y^{(3)}/6]\right\}/8 \\ I^{\beta}_{ijk}(v) &= [\beta(v_{ijk} + v_{i-1,j,k}) + (1-\beta)(v_{i,j+1,k} + v_{i-1,j+1,k})]/2 \end{aligned} \tag{8}$$

where $\delta x_i = x_i - x_{i-1}$, $\beta = \delta y_{j+1}/(\delta y_j + \delta y_{j+1})$. $o(\epsilon^4)$ denotes a fourth order cut-off error, R_{ijk} represents the remainder resulted from linear interpolation in terms of operator (I^{β}_{ijk}). The difference from the previous scheme given in Ref. [41] lies in the deduction of this interpolation remainder, which has obviously enhanced the accuracy of finite difference for the cross-convection term vu_y. Clearly, similar expressions can be derived for the finite difference of other cross-convection terms, i.e. wu_z in the streamwise momentum equation, $[uv_x, wv_z]$ in the transverse momentum equation and $[uw_x, vw_y]$ in spanwise momentum equation.

In addition, for the calculation of intermediate velocities, the convection terms were treated explicitly, and calculated by a blocked tri-diagonal matrix acceleration (TDMA) in the streamwise direction due to the periodic boundary condition. The pressure potential Poisson's equation was solved by the approximate factorization one (AF1) method [51]. The streamwise periodicity of pressure potential was appropriately considered in the AF1 iteration.

The temperature equation (2) was solved by time marching. The implicit second-order Crank–Nicolson for the right-hand side diffusion terms, and fourth-order upwind scheme for the left-hand side convection terms were used in spatial discretization. The left-hand side term corresponding to the streamwise variation of duct wall temperature was treated together with the convective terms by using the third order Adams–Bashforth scheme in temporal discretization.

4. Results and discussion

The c-DNS for the turbulent forced heat convection in the SSD was carried out in the staggered grid system with the grid density adjusted with a power law and higher grid density near the duct wall. The streamwise grid is nearly uniform, its grid number was 121, and both the transverse and spanwise grid numbers were equal to 101. The streamwise length of the computational domain is equal to $6.41H$. The Reynolds number based on the side of square duct section and bulk velocity was 10^4. The convergence criterion for pressure potential iteration was chosen so that the relative error defined previously [52] should be less than 3×10^{-8}. The c-DNS highlights the following issues:

- Predict the time mean and local Nusselt numbers and their root mean square values for the turbulent forced heat convection in the SSD under an isoflux peripheral wall heating mode, and further evaluate the corresponding availability of the novel turbulence model based on the nonstandard analysis.
- Explore the characteristics of velocity and temperature fluctuations in the turbulent SSD flow, while keeping the numerical viscous effect as low as possible by recruiting grid-dependent terms with respect to Taylor expansion.

4.1. Turbulence statistics

Since the flow in the streamwise direction is homogeneous, turbulence statistical values were evaluated by averaging in time and x.

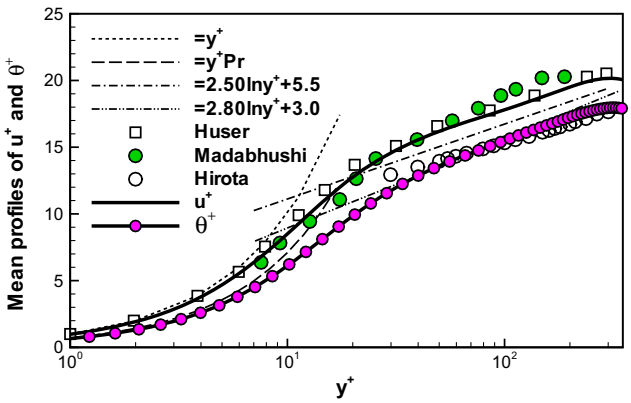

Fig. 1. The mean velocity and temperature profiles along the wall bisector plotted as a function of the wall coordinate. Note that $\bar{\theta}^+ \equiv 13\bar{\Theta}^+$, $y^+ = (y + 0.5)u_\tau/\nu$, and the over-bar means the time and x-average. The friction Reynolds number based on H is 360 in the LES of Madabhushi and Venka [13], 600 in the semi-spectral DNS of Huser and Biringen [21], and is 612.4 in the present study. The bulk Reynolds number in the heat transfer experiment of Hirota et al. [55] is 6.7×10^4.

The time range used in the average was from $t = 300$ to 500, in which a data sequence with five 10 thousand records was used in the analysis of turbulence statistics.

The predicted mean friction factor f is about 0.030, implying that the mean wall shear velocity is linked to the bulk velocity by ratio $u_\tau/U_m = \sqrt{f/8} = 0.06124$. This wall shear velocity is used as another velocity scale in results shown in Figs. 1 and 3.

Plotted as the functions of the wall coordinate (y^+), the mean velocity and the temperature profiles along the wall bisector are given in Fig. 1. In the core region of the SSD flow, $30 \leqslant y^+ \leqslant \mathrm{Re}_\tau/2$, the predicted mean velocity follows a log-law with a constant terms of about 7.5 rather than 5.5 in the log-law of turbulent plane channel flow illustrated by dash-dotted line. In the sublayer, $0 < y^+ \leqslant 5$, the predicted mean velocity satisfies the linear wall law illustrated by dashed curve. In the buffer region, $5 < y^+ \leqslant 30$, the predicted solid curve passes through the gap between the small squares and filled circles, which represent the results of recently published LES and DNS. Since the friction Reynolds number used in the present study is almost the same as the one considered in the previous DNS [21], the velocity profile fits with the results from the previous DNS quite well. The comparison observed in Fig. 1 indicates that the present c-DNS can evidently predict the mean velocity profile consistently well with the existing results of computations.

For the mean profile $\bar{\theta}^+$, the slope (2.80) of the log-law in the core region is very close to the slope (2.78) found in the turbulent heat transfer in channel flows [28]. Similar to velocity profile, we have estimated a larger constant in the log-law, 3.0, as compared to the log-law constant of Kasagi et al. 2.09. The comparison of mean profile of θ^+ with the previous measurement [55,54] is fairly good. The reason that leads to the deviation in comparison may come from difference in wall heating condition. In the numerical prediction, the streamwise heating length is assumed to be infinitive due to the use of periodic condition, while in experiment, the heating length is limited.

It is noted that the temperature at a given point in the computational domain shows a linear increase trend with time in addition to its irregular turbulent fluctuation (Fig. 10) due to the constant heating from the SSD walls. The output data analysis shows that the increase rate of mean temperature ($\bar{\Theta}^+$) is *roughly* equal to $4u_\tau\bar{u}/(30 \times 13U_m)$. Using this particular increase rate, data analysis can output the mean temperature profile insensitive to the time average period.

The velocity variation bands in the unit of their root mean square values along the wall bisector was shown in Fig. 2 where the velocity bands $[u] = \max(u) - \min(u)$, and $[v] = \max(v) - \min(v)$, in which u and v denotes the x-averaged velocities. The velocity peaks were adjusted so that their mid points have the corresponding mean values. It reveals that the chance of velocity fluctuations beyond 2.5 is very small.

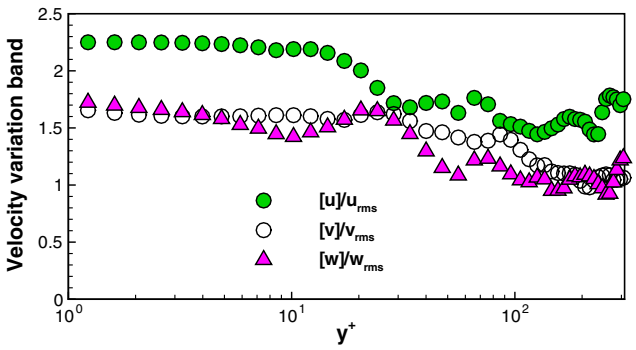

Fig. 2. The velocity variation band plotted as a function of the wall coordinate.

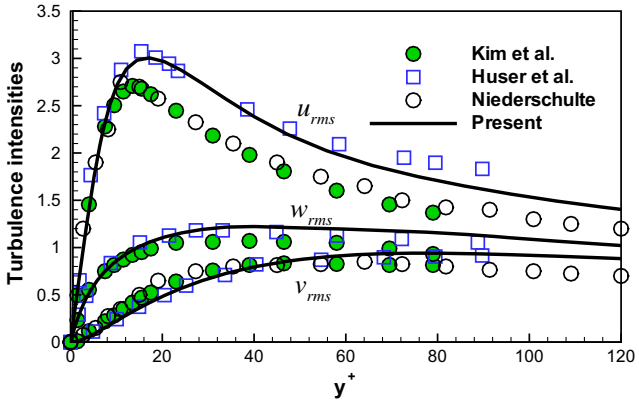

Fig. 3. Turbulence intensities along the wall bisector plotted as a function of the wall coordinate. Note that the friction Reynolds number is 180 (based on the channel half-width and wall shear velocity) in the fully spectral DNS of the plane channel flow done by Kim et al. [26], and in the experiment with laser-Doppler techniques by Niederschulte et al. [33].

The root mean square (rms) values of velocities given in Fig. 3, which show the characteristics of the secondary flows in the SSD flows, have shown a fairly good agreement with the existing numerical results. The reason causing the visible deviations from the channel flow c-DNS can be the difference in the Reynolds number and the flow geometry. The rms of θ^+ along the wall bisector is shown by the coarse solid curve in Fig. 4. Comparison was made between the DNS in Ref. [28]. It is seen that, in the sublayer, the currently predicted rms value of θ^+ is slightly higher than that from the previous DNS for heat transfer in channel flow. Visible deviation occurs in the buffer and the core regions. Another reason is the differences in the solution method, in which the approach of discretizing the convection terms in the governing equations has a significant impact on variables' rms values, as reported by Liang et al. [23].

Since the flow is at a large Reynolds number, lower order schemes in discretization usually introduce grid-dependent artificial viscous terms, providing a spurious-nonphysical mechanism to suppress the turbulence fluctuations. In the present simulation, the recruiting grid-dependent terms are derived and used to decrease the artificial viscous effect.

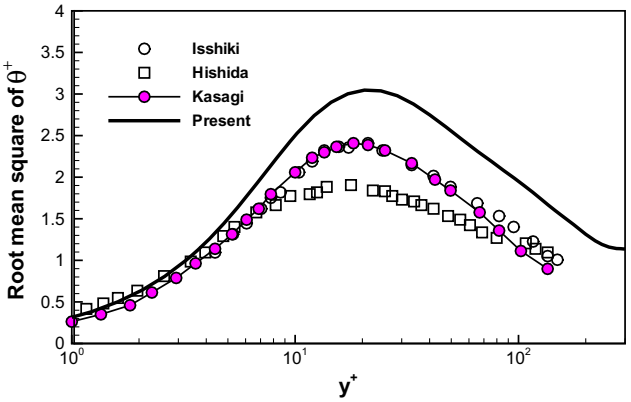

Fig. 4. Root mean square of θ^+ along the wall bisector plotted as a function of the wall coordinate. Note that the friction Reynolds number is 150 (based on the channel half-width and wall shear velocity) in the fully spectral DNS of the plane channel flow done by Kasagi et al. [28], and the data labeled by 'Isshiki' abstracted indirectly from [28]. The friction Reynolds number in the work of Hishida et al. [53] is 879.

4.2. Heat transfer

Assuming that the time mean temperature of the air in the domain is denoted by $T_{m,av}$, the mean Nusselt number of the forced heat convection in the SSD can be written as

$$\overline{Nu}_{av} = \frac{13T_\tau}{\overline{T}_w - T_{m,av}} \frac{1}{4} \int_\Gamma \frac{\partial \bar{\Theta}^+}{\partial n} d\Gamma \tag{9}$$

where Γ is the boundary of the cross-section, and $\mathbf{n}$ is the corresponding inner normal unit vector of Γ. The present DNS shows that the mean Nusselt number in the case of isoflux wall heating is 29.38, which is in an excellent agreement with the mean Nusselt number (28.49) based on the Gnielinski's empirical expression for the turbulent forced heat convection in a circular pipe [56], which had some theoretical foundation in a low-Reynolds number correction. The Gnielinski's empirical expression is

$$Nu = \frac{(\mathrm{Re} - 1000)\mathrm{Pr}\, c_f/2}{1.0 + 12.7\sqrt{c_f/2}(\mathrm{Pr}^{2/3} - 1.0)} \tag{10}$$

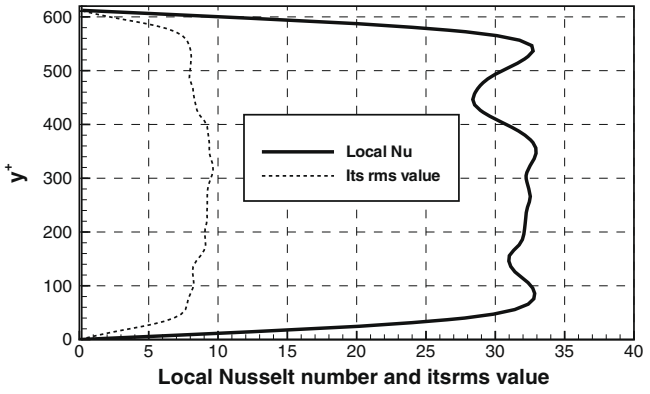

Fig. 5. The mean local Nusselt number and its rms value plotted as a function of y^+. Note that the mean local Nusselt number is defined by $\overline{Nu}(y) = \{\overline{Nu}|_{z=-0.5} + \overline{Nu}|_{z=+0.5}\}/2$; the over-bar represents the time and x-average.

which is available in the ranges: $0.5 < \mathrm{Pr} < 2000$, and $2300 < \mathrm{Re} < 5 \times 10^6$, here $c_f = f/4$, and f is the friction factor. The mean Nusselt number should be 29.78, if calculated by the empirical correlation of Sleicher and Rouse [57]

$$Nu = 5 + 0.015\mathrm{Re}^a \mathrm{Pr}^b \tag{11}$$

with

$$a = 0.88 - 0.24/(4 + Pr), \quad b = 0.333 + 0.5e^{-0.67Pr}$$

for the valid ranges of Pr and Re given by $0.1 < \mathrm{Pr} < 10^4$, and $10^4 < \mathrm{Re} < 10^6$. A comparison shows that the relative deviation is less than 5%.

Shown in Fig. 5, are the mean local Nusselt number and its rms curves plotted as functions of the transverse coordinate. In the central region, $60 \leqslant y^+ \leqslant 552.4$, the local Nussel number distributes around the mean value 29.38 in the rise and fall manner. It tends to zero in a rapid decreasing rate when the wall coordinate gradually closes to the corner points of the SSD. The wavy distribution of mean local heat flux is closely dependent on the near wall turbulence (Fig. 6(a)–(d)), its rms value is at a level of 25% of the mean local Nusselt number in the central region, implying that the heat transfer through the duct wall should have experienced an intensively irregular oscillating mode. A recent detail numerical study for channel flow presents a similar evidence, and the results revealed the characteristics of the near wall heat flux [58].

4.3. Turbulent flow fields

Effects on the turbulent flow in a SSD come from the four duct walls and the wall right corners. The merging of the four boundary layers is influenced by the mean secondary flow in Fig. 7(a). Here the mean includes the quadrant average with respect to the center of the cross-section. It is seen in Fig. 7(a) that the mean secondary vortex pairs are concentrated in the corner region, and distributed symmetrically to the corner bisector.

To improve the understanding of the SSD flow, it would be helpful to review the coherent motion in shear flow [59]. The previous visualization for mixing layer of Bernal and Roshko in 1986 indicated that a single row of counter-rotating vortices appeared in a

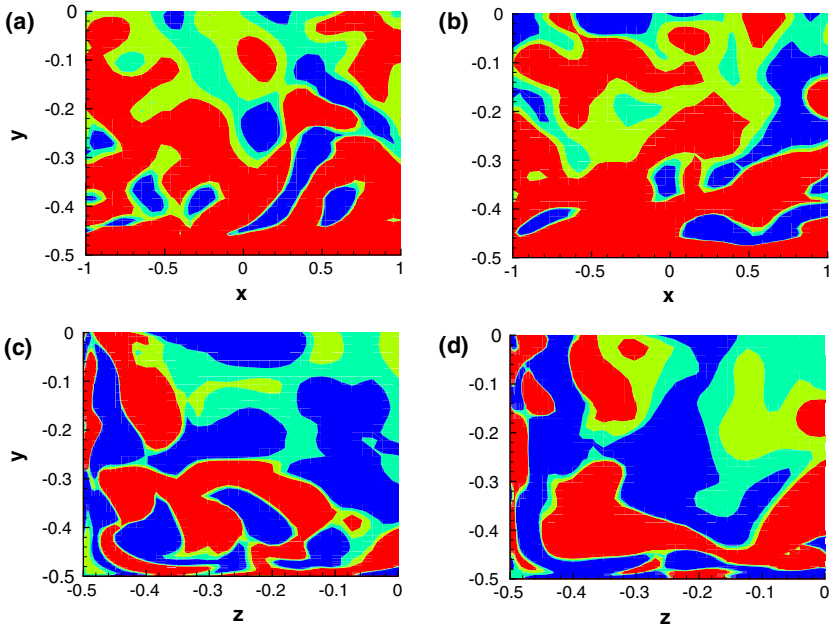

Fig. 6. Instantaneous ω_3 fields in the slice of $z = 0$ and ω_1 fields in the slice of $x = 0$. (a) $\omega_3, t = 400$; (b) ω_3, $t = 410$; (c) $\omega_1, t = 400$ and (d) $\omega_1, t = 410$. Note that the vortices are labeled by vorticity values −0.5, 0, and 0.5.

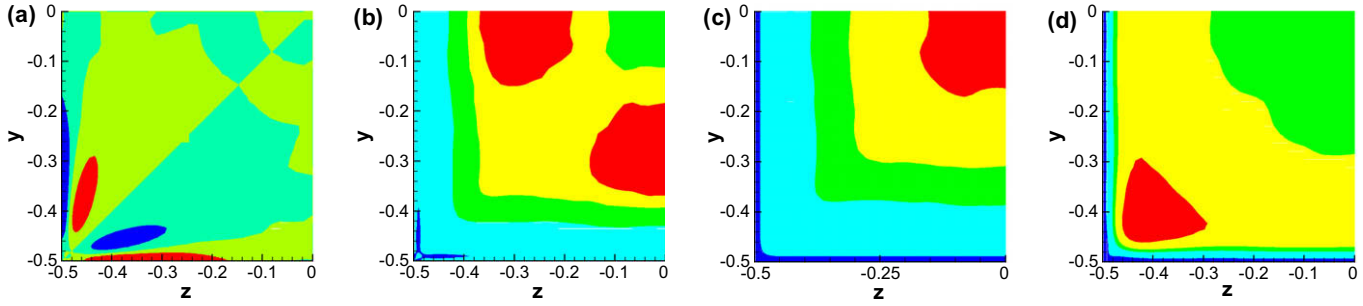

Fig. 7. Distributions of $\overline{\omega}_1$(a), the fluctuation vorticitiy ratio $\omega'_{1\mathrm{rms}}/\omega'_{\mathrm{rms}}$(b), the $\log(\tau_u)$, and the time scale ratio $R=\tau_\theta/\tau_u$. Note that $\overline{\omega}_1$ in (a) are labeled by vorticity values −0.5, 0, and 0.5; $\omega'_{1\mathrm{rms}}/\omega'_{\mathrm{rms}}$ in (b) is labeled by 0.25, 0.5, $1/\sqrt{3}$ and 0.6; $\log(\tau_u)$ in (c) is labeled by −1, 0, 0.2 and 0.4; and R in (d) is labeled by 0.71, 0.9, 1, 1.2.

slice through a braid, and two rows of counter-rotating vortices located on the top and bottom of the spanwise vortex core in a slice through the vortex core.

For the flow near the bottom wall, two snapshots are made to show the spanwise vortex structures in the slice of $z=0$ (Fig. 6(a) and (b)), with the corresponding instantaneous secondary vortex structures shown in Fig. 6(c) and (d) for the comparison convenience. In Fig. 6(a) and (b), prograde vortices are red[2] colored, and retrograde vortices are blue colored. According to the recent vortex signature study [60,61], it is revealed that there are two prevailing retrograde vortex orientations: (1) in the third quadrant of a prograde vortex core, (2) in the first quadrant of a prograde vortex core. The former corresponds to the motion of omega-shaped hairpin vortices, and the latter corresponds to the motion detached-ring like structures. In Fig. 6(a), it can be seen that in the bottom layer, the prograde voetex is prevailing due to the wall effect, and a retrograde usually surrounded by several prograde vortices, indicating that the SSD flow has a property of vortical structure transportation. In Fig. 6(b), at the instant of $t=410$, a spanwise vortex ring appears and encloses a retrograde vortex.

As shown in Fig. 6(c) and (d), the coherent secondary motion in the slice of $x=0$ is found to be more intensive as compared with the mean motion in Fig. 7(a). The instantaneous secondary vortices can distribute in the whole cross-section, their motion is coherently involved with the spanwise vortex organizations as shown in Fig. 6(a) and (b).

Together with the mean secondary flow given in Fig. 7(a), distributions of the fluctuation vorticity ratio, the logarithm of turbulence time scale, and the ratio between the temperature and velocity dissipation time scales are shown Fig. 7(b)–(d). The turbulence time scale τ_u was defined by

$$\tau_u=\frac{3}{2}C_D k_u/\epsilon_u \tag{12}$$

here $C_D=0.09$ is a commonly used coefficient in phenomenological turbulence models [62]. ν is the kinematic viscosity of fluid. The turbulence kinetic energy k_u and its dissipation rate were defined by [63]

$$k_u=0.5\overline{u'_j u'_j}, \tag{13}$$

$$\epsilon_u=2\nu\overline{s_{ij}s_{ij}},\quad s_{ij}=(\partial u'_i/\partial x_j+\partial u'_j/\partial x_i)/2 \tag{14}$$

where s_{ij} is the tensor of deformation rate fluctuation. The time scale of temperature dissipation was defined by

$$\tau_\theta=\frac{3}{2}C_D k_\theta/\epsilon_\theta \tag{15}$$

where

$$k_\theta=0.5\overline{(\theta')^2},\quad \epsilon_\theta=\mathrm{Pr}^{-1}\nu\overline{(\partial\theta'/\partial x_j)^2} \tag{16}$$

Here the superscript '+' is omitted in the definition of k_θ and ϵ_θ, since the temperature normalization does not affect the time scale. The time ratio R is not coupled with coefficient C_D, and R is simply given by

$$R=\tau_\theta/\tau_u \tag{17}$$

As seen in Fig. 7(b)–(d), the mean secondary flow has some influence on the distributions of the fluctuation vorticity ratio $\omega_{1\mathrm{rms}}/\omega_{\mathrm{rms}}$ and turbulence time scale $\log(\tau_u)$, but a more evident effect on the time scale ratio. It causes a significant increase of R in the corner region between the two mean secondary vortices near the corner bisector.

The illustration of the mean and instantaneous flow fields and the distributions of some turbulence variables is useful for recognizing some speciality of the turbulent SSD flow at the $\mathrm{Re}=10^4$.

4.4. Velocity and temperature fluctuations

Corresponding to the intensively changing turbulent flow fields, are the significant fluctuations of velocity and temperature of fluid particles, for those positioned in the wall bisector, the rms curves have been shown in Figs. 3 and 4. Further, the predicted probability density functions (PDFs) characterizing the variable fluctuation behaviors are shown in Figs. 8 and 9, where $u_r=(u-0.5[u])/[u]$, $v_r=(v-0.5[v])/[v]$, the velocity bands $[u]=\max(u)-\min(u)$, and $[v]=\max(v)-\min(v)$ are the same as in Fig. 2. Here u, v have the streamwise averaged values. The multiple spikes in the PDFs of the streamwise velocity (Fig. 8(a)) indicate the complexities of the duct flow, implying the SSD flow has the low-speed and high-speed streamwise streaks. The PDFs in Fig. 8(a) and (b) suggest that the velocity fluctuates with less relationship with Gaussian distribution.

The joint behavior of velocity fluctuations can be observed in Fig. 9. The joint PDF is useful for the *quadrant analysis* of motion events of fluid particle near the observed points. For the case of $y^+=5.88$ on the wall bisector, as shown in Fig. 9(a), large fluctuation behaviors are mainly concentrated in the second and fourth quadrant events, indicating that the large amplitude fluid ejections (the second quadrant events) and sweeps (the fourth quadrant event) are the prevailing events, which give rise to a positive Reynolds shear stress $(-\overline{uv})$ at the observed point. The smaller fluctuations around the origin of the re-scaled velocity plane (u_r, v_r) follow the joint PDF whose shape likes an hilly island, around which are many granular planet islands. This means that large amplitude velocity fluctuations are associated with the coherent motions of larger vortices.

The joint velocity fluctuation behavior at $y^+=14.49$ given in Fig. 9(b) is similar to that shown in Fig. 9(a) for the behavior at

[2] For interpretation of the references to color in this figure, the reader is referred to the web version of this article.

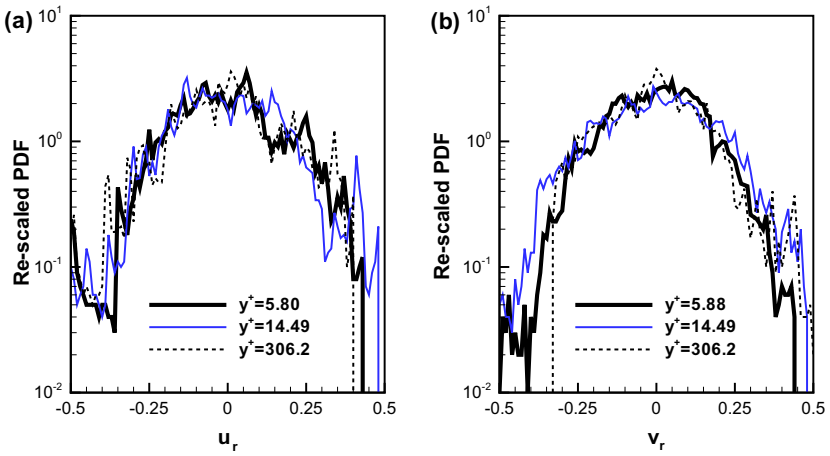

Fig. 8. Re-scaled probability density function (PDF) plotted as the re-scaled velocities at various positions of the wall bisector. (a) PDF of u_r and (b) PDF of v_r.

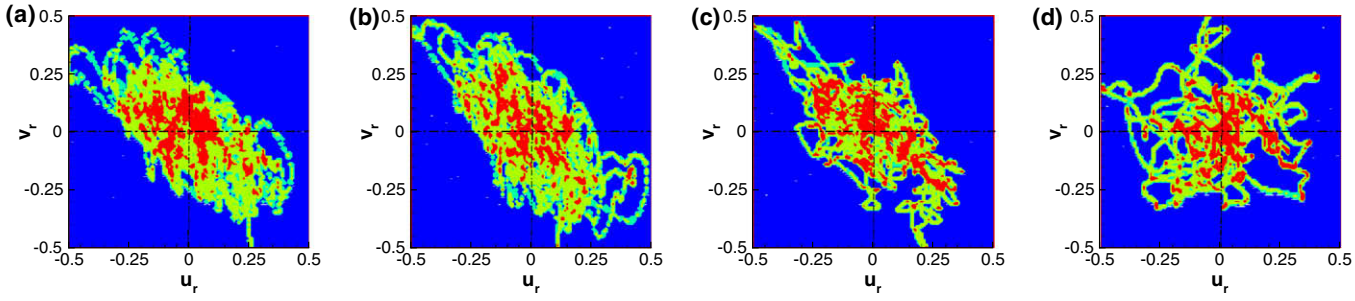

Fig. 9. Re-scaled joint probability density function in the re-scaled velocity plane at various position along the wall bisector. Note that the figures (a–d) show contours at y^+ = 5.88, 14.49, 65.80, and 306.2, respectively; and the contours are labeled by 0.1, 1, and 5.

$y^+ = 5.88$. The prevailing of the ejection and sweeps again indicates the Reynolds shear stress is positive. In the active coherent motion region, $y^+ = 65.80$, as indicated in Fig. 9(c), the joint velocity fluctuation prefers to follow some orbits in the plane, showing that such fluctuations contain recurrence feature. The traces of the velocity fluctuation in Fig. 9(d) look like some worm-creeps. Since the point at $y^+ = 306.2$ in the wall bisector just overlaps the duct section center, the Reynolds shear stress is zero. The large deviation of shear stresses does not indicate that the instantaneous streamwise momentum flux transported by the transverse velocity fluctuation at the point is zero.

The joint PDF distributed zone appears in about elliptic form, the cross-angle between the primary axis of the ellipse and the vertical coordinate decreases with the distance from the wall. This indicates that the quadrant events near wall have smaller vertical velocity fluctuation, with the increase of the distance from the wall, the re-scaled vertical velocity fluctuation gradually becomes comparable with the re-scaled streamwise velocity fluctuation.

As shown in Fig. 10, at the two points labeled by $y^+ = 18.4$ and 306.2 on the wall bisector in the streamwise mid cross-section ($x = 0$), the values of Θ^+ occur irregularly fluctuate, with those in the time period $t \in (480, 500)$ zoomed in the right-upper corner. Subjecting the effect from the coherent structures in the buffer layer $y^+ \in (5, 30)$ defined in Ref. [63], the temperature at $y^+ = 18.4$ fluctuates in a larger magnitude and a lower primary frequency, as compared to the fluctuation in the core region point ($y^+ = 306.2$). These properties of temperature fluctuation can also be observed in the corresponding diagram of power spectra versus frequency (Fig. 11), which was obtained by a code based on the Hilbert transform [64]. The power spectrum analysis shows that the oscillation in the buffer region has larger power spectrum values

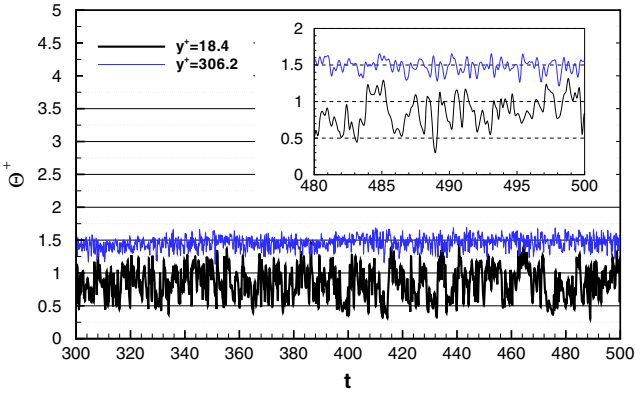

Fig. 10. Evolutions of normalized temperature at two points on the wall bisector ($z = 0$) in the mid cross-section ($x = 0$): y^+=18.4, and 306.2.

(or larger magnitudes), the frequency band is between 0.01 and 5. The frequencies relevant to the temperature oscillation at the inertia range is around 2. The approximated inertia range of frequency is about from 1 to 2.5, suggesting that the fluctuation with a frequency lower than (U_m/H) can be seen as low frequency oscillation, with those over $(2.5U_m/H)$ taken as higher frequency oscillation.

Due to constant heating, and the periodic streamwise condition for Θ^+, the time average temperature is dependent on the time period (Fig. 10), this effect of mean temperature increase should be erased properly in output data analysis. We assume the increase rate of the mean temperature is proportional to $\frac{4u_\tau}{13U_m}\bar{u}$, by analysis,

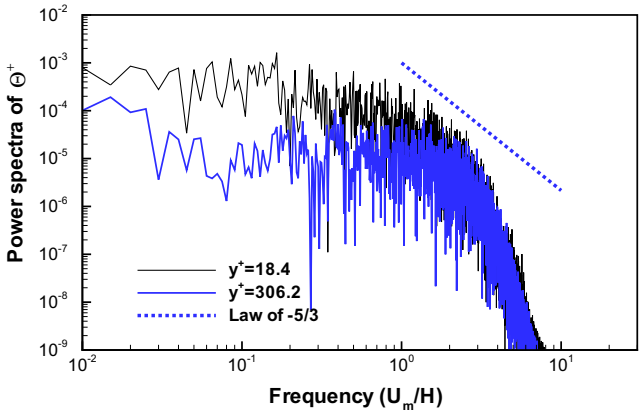

Fig. 11. The power spectra corresponds to the temperature evolutions shown in Fig. 10.

it was found that the proportionality is roughly 1/30, which allows to obtain the mean temperature that is insensitive to the time period in averaging.

5. Conclusions

An improved finite difference of the cross-convection terms in the governing equations of turbulent flows is reported in the c-DNS of the turbulent forced heat convection in a SSD at a bulk Reynolds number of 10^4. The novel scheme is more stable and is found to be applicable in capturing the turbulence characteristics of the SSD flow, which has avoided the interruption of artificial viscosity as far as possible. Using the recent nonstandard analysis of turbulence, the c-DNS can be performed by recruiting the grid-dependent interpolation remainder in the calculation of the cross-velocities. The computed mean Nusselt number is in an excellent agreement with the value based on the published correlations, with a relative standard deviation less than 5%. The mean secondary flow significantly increases the ratio between the temperature and velocity dissipation time scales in the corner region between the mean secondary counter-rotating vortices. The probability density functions have been calculated to help understanding of velocity fluctuation behaviors. The power spectrum diagram of temperature show that the frequency band is between 0.01 and 5, with the inertia range about from 1 to 2.5. The satisfactory agreement with the existing DNS results from other numerical schemes suggests that the novel finite difference scheme has potentials for efficient and accurate turbulence prediction because of the higher-precise calculation of the cross-velocities.

Acknowledgments

This work was funded by the donation from the Sun Hong Kai Properties Group. We also wish to acknowledge the support of S.L. Xu in USTC, and the support of NSFC (10572135).

References

[1] P. Bradshaw, Turbulent secondary flows, Annu. Rev. Fluid Mech. 19 (1987) 53–74.
[2] Z.H. Qin, R.H. Pletcher, Large eddy simulation of turbulent heat transfer in a rotating square duct, Int. J. Heat Fluid Flow 27 (2006) 371–390.
[3] E. Brundrett, W.D. Baines, The production and diffusion of vorticity in duct flow, J. Fluid Mech. 19 (1964) 375–394.
[4] F.B. Gessner, J.B. Jones, On some aspects of fully-developed turbulent flow in rectangular channels, J. Fluid Mech. 23 (1965) 689–713.
[5] F.B. Gessner, The origin of secondary flow in turbulent flow along a corner, J. Fluid Mech. 58 (1973) 1–25.
[6] A. Melling, J.H. Whitelaw, Turbulent flow in a rectangular duct, J. Fluid Mech. 78 (1976) 289–315.
[7] A. Nakayama, W.L. Chow, D. Sharma, Calculation of fully developed turbulent flows in ducts of arbitrary cross-section, J. Fluid Mech. 128 (1983) 199–217.
[8] G. Yang, M.A. Ebadian, Effect of Reynolds and Prandtl numbers on turbulent convective heat transfer in a three-dimensional square duct, Numer. Heat Transfer A: Appl. 20 (1991) 111–122.
[9] A. Saidi, B. Sundén, Numerical simulation of turbulent convective heat transfer in square ribbed ducts, Numer. Heat Transfer A: Appl. 38 (1) (2000) 67–88.
[10] K. Tatsumi, H. Iwai, K. Inaoka, K. Suzuki, Numerical analysis for heat transfer characteristics of an oblique discrete rib mounted in a square duct, Numer. Heat Transfer A: Appl. 44 (8) (2003) 811–831.
[11] T.T. Wong, C.W. Leung, Z.Y. Li, W.Q. Tao, Turbulent convection of air cooled rectangular duct with surface-mounted cross-ribs, Int. J. Heat Mass Transfer 46 (2003) 4629–4638.
[12] A. Valencia, Turbulent flow and heat transfer in a channel with a square bar detached from the wall, Numer. Heat Transfer A: Appl. 37 (3) (2000) 289–306.
[13] R.K. Madabhushi, S.P. Vanka, Large eddy simulation of turbulence-driven secondary flow in a square duct, Phys. Fluids A 3 (11) (1991) 2734–2745.
[14] M.D. Su, R. Friedrich, Investigation of fully developed turbulent flow in a straight duct with large eddy simulation, ASME J. Fluid Eng. 116 (4) (1994) 677–684.
[15] M.S. Vázquez, O. Métais, Large-eddy simulation of the turbulent flow through a heated square duct, J. Fluid Mech. 453 (2002) 201–238.
[16] O. Métais, M. Lesieur, New trend in large eddy simulation of turbulence, Annu. Rev. Fluid Mech. 28 (1996) 45–82.
[17] E. Lamballais, M. Lesieur, O. Métais, Probability distribution function and coherent structures in a turbulent channel, Phys. Rev. E 56 (1997) 6761–6766.
[18] J. Pallares, L. Davidson, Large-eddy simulations of turbulent flow in a rotating square duct, Phys. Fluids 12 (2000) 2878–2894.
[19] J. Pallares, L. Davidson, Large-eddy simulations of turbulent heat transfer in stationary and rotating square ducts, Phys. Fluids 14 (2002) 2804–2816.
[20] S. Gavrilakis, Numerical simulation of low-Reynolds-number turbulent flow through a straight square duct, J. Fluid Mech. 244 (1992) 101–129.
[21] A. Huser, S. Biringen, Direct numerical simulation of turbulent flow in a square duct, J. Fluid Mech. 257 (1993) 65–95.
[22] Y. Joung, S.U. Choi, J.I. Choi, Direct numerical simulation of turbulent flow in a square duct: analysis of secondary flows, ASCE J. Eng. Mech. 133 (2) (2007) 213–221.
[23] D. Liang, Z.Y. Li, W.Q. Tao, The application of high resolution finite difference scheme in direct numerical simulation of turbulent flow, J. Eng. Thermophys. 28 (5) (2007) 859–861 (in Chinese).
[24] W.P. Wang, R.H. Pletcher, On the large eddy simulation of a turbulent channel flow with significant heat transfer, Phys. Fluids 8 (1996) 3354–3366.
[25] L.D. Dailey, N. Meng, R.H. Pletcher, Large eddy simulation of constant heat flux turbulent channel flow with property variations: Quasi-developed model and mean flow results, ASME J. Heat Transfer 125 (2003) 27–38.
[26] J. Kim, P. Moin, R. Moser, Turbulence statistics in fully developed channel flow at low Reynolds number, J. Fluid Mech. 177 (1987) 133–166.
[27] B.Y. Li, N.S. Liu, X.Y. Lu, Direct numerical simulation of wall-normal rotating turbulent channel flow with heat transfer, Int. J. Heat Mass Transfer 49 (2006) 1162–1175.
[28] N. Kasagi, Y. Tomita, A. Kuroda, Direct numerical simulation of passive scalar field in a turbulent channel flow, ASME J. Heat Transfer 114 (1992) 598–606.
[29] N. Kasagi, N. Shikazono, Contribution of direct numerical simulation to understanding and modelling turbulent transport, Proc. R. Soc. Lond. A 45 (1995) 257–292.
[30] N. Kasagi, N. Shikazono, Direct numerical simulation of combined forced and natural turbulent convection in a vertical plane channel, Int. J. Heat Fluid Flow 18 (1997) 88–99.
[31] H.P. Kreplin, H. Eckelmann, Behavior of the three fluctuating velocity components in the wall region of a turbulent channel flow, Phys. Fluids 22 (1979) 1233–1239.
[32] T. Wei, W.W. Willmarth, Reynolds number effects on the structures of a turbulent channel flow, J. Fluid Mech. 204 (1989) 57–95.
[33] M.A. Niederschulte, R.J. Adrian, T.J. Hanratty, Measurement of turbulent flow in a channel at low Reynolds numbers, Exp. Fluids 9 (1990) 222–230.
[34] I.N. Wardana, T. Ueda, M. Mizomoto, Effect of strong heating on turbulence statistics of a channel flow, Exp. Fluids 18 (1994) 87–94.
[35] H.X. Yang, Z.J. Zhu, Numerical study of turbulent Rayleigh–Benard convection, Int. Commun. Heat Mass Transfer 33 (2006) 184–190.
[36] H.X. Yang, Z.J. Zhu, Numerical study of three-dimensional turbulent natural convection in a differentially heated air-filled tall cavity, Int. Commun. Heat Mass Transfer 35 (2008) 606–612.
[37] F. Wu, Non-standard picture of turbulence, 2004 (Preprint at http://arXiv:physics/0308012).
[38] F. Wu, Some key concepts in nonstandard analysis theory of turbulence, Chin. Phys. Lett. 22 (2005) 2604–2607.
[39] F. Wu, Mathematical concepts and their physical foundation in the nonstandard analysis theory of turbulence, Chin. Phys. 16 (2007) 1186–1196.
[40] J. Salat, S.H. Xin, P. Joubert, F. Penot, P. Le Quéré, Experimental and numerical investigation of turbulent natural convection in a large air-filled cavity, Int. J. Heat Fluid Flow 25 (2004) 824–832.
[41] J.L. Niu, Z.J. Zhu, Numerical study of three-dimensional flows around two identical square cylinders in staggered arrangements, Phys. Fluids 18 (4) (2006) 044106.

[42] R.D. Moser, J. Kim, N.N. Mansour, Direct numerical simulation of turbulent channel flow up to $Re_\tau = 590$, Phys. Fluids 11 (4) (1999) 943–945.
[43] P. Le Quéré, T.A.D. Roquefort, Computation of natural convection in two-dimensional cavities with Chebyshev polynomials, J. Comput. Phys. 57 (1985) 210–228.
[44] N. Nikitin, Finite-difference method for incompressible Navier–Stokes equations in arbitrary orthogonal curvilinear coordinates, J. Comput. Phys. 217 (2006) 759–781.
[45] S.V. Patankar, Numerical Heat Transfer and Fluid Flow, Hemisphere, New York, 1980.
[46] E. Papanicolaou, Y. Jaluria, Transition to a periodic regime in mixed convection in a square cavity, J. Fluid Mech. 239 (1992) 489–509.
[47] K. Khanafer, K. Vafai, M. Lightstone, Mixed convection heat transfer in two dimensional open-ended enclosures, Int. J. Heat Mass Transfer 45 (26) (2002) 5171–5190.
[48] B.I. Shraiman, D.E. Siggia, Scalar turbulence, Nature 405 (2000) 639–646.
[49] D.L. Brown, R. Cortez, M.L. Minion, Accurate projection methods for the incompressible Navier–Stokes equations, J. Comput. Phys. 168 (2001) 464–499.
[50] H.X. Yang, Z.J. Zhu, Exploring super-critical properties of secondary .ows of natural convection in inclined channels, Int. J. Heat Mass Transfer 47 (2004) 1217–1226.
[51] T.J. Baker, Potential flow calculation by approximation factorization method, J. Comput. Phys. 42 (1981) 1–19.
[52] Z.J. Zhu, H.X. Yang, Numerical investigation of transient laminar natural convection of air in a tall cavity, Heat Mass Transfer 39 (2003) 579–587.
[53] M. Hishida, Y. Nagano, M. Tagawa, Transport process of heat and momentum in the wall region of turbulent pipe flow, in: C.L. Tian (Ed.), Proceedings of the 8th International Heat Mass Transfer Conference, vol. 3, Hemisphere, Washington, 1986, pp. 925–930.
[54] M. Hirota, H. Fujita, H. Yokosawa, Experimental study on convective heat transfer for turbulent flow in a square duct with robbed rough wall (characteristics of temperature field), ASME J. Heat Transfer 116 (1994) 332–340.
[55] M. Hirota, H. Fujita, H. Yokosawa, H. Nakai, H. Itoh, Turbulent heat transfer in a square duct, Int. J. Heat Fluid Flow 18 (1997) 170–180.
[56] W. Kays, M. Crawford, B. Weigand, Convective Heat and Mass Transfer, fourth ed., McGraw-Hill, New York, 2005. p. 299.
[57] C.A. Sleicher, M.W. Rouse, A convenient correlation for heat transfer to constant and variable properties fluids in turbulent pipe flow, Int. J. Heat Mass Transfer 18 (1975) 677–683.
[58] H. Abe, H. Kawamura, Y. Matsuo, Surface heat flux fluctuations in a turbulent channel flow up to $Re_\tau = 1020$ with $Pr = 0.025$ and 0.71, Int. J. Heat Fluid Flow 25 (2004) 404–419.
[59] L.P. Bernal, A. Roshko, Streamwise vortex structure in plane mixing layers, J. Fluid Mech. 170 (1986) 499–525.
[60] R.J. Adrain, C.D. Meinhart, C.D. Tomkins, Vortex organization in the outer region of the boundary layer, J. Fluid Mech. 422 (2000) 1–54.
[61] V.K. Natrajan, Y. Wu, K. Christensen, Spatial signatures of retrograde spanwise vortices in wall turbulence, J. Fluid Mech. 574 (2007) 155–167.
[62] K. Hanjalic, One-point closure model for buoyancy driven turbulent flows, Annu. Rev. Fluid Mech. 34 (2002) 321–347.
[63] H. Tennekes, J.L. Lumley, A First Course in Turbulence, MIT Press, Cambridge, 1974. pp. 146–195.
[64] Z.J. Zhu, H.X. Yang, Discrete Hilbert transformation and its application to estimate the wind speed in Hong Kong, J. Wind Eng. Ind. Aerodyn. 90 (1) (2002) 9–18.